Chemical Science

ROYAL SOCIETY OF CHEMISTRY

EDGE ARTICLE

View Article Online
View Journal | View Issue

Cite this: *Chem. Sci.*, 2022, **13**, 3719

All publication charges for this article have been paid for by the Royal Society of Chemistry

Suppressing thermal quenching of lead halide perovskite nanocrystals by constructing a wide-bandgap surface layer for achieving thermally stable white light-emitting diodes†

Qinggang Zhang,[ab] Mengda He,[a] Qun Wan,[a] Weilin Zheng,[a] Mingming Liu,[a] Congyang Zhang,[a] Xinrong Liao,[a] Wenji Zhan,[a] Long Kong,[a] Xiaojun Guo[b] and Liang Li*[ac]

Lead halide perovskite nanocrystals as promising ultrapure emitters are outstanding candidates for next-generation light-emitting diodes (LEDs) and display applications, but the thermal quenching behavior of light emission has severely hampered their real-world applications. Here, we report an anion passivation strategy to suppress the emission thermal quenching behavior of $CsPbBr_3$ perovskite nanocrystals. By treating with specific anions (such as SO_4^{2-}, OH^-, and F^- ions), the corresponding wide-bandgap passivation layers, $PbSO_4$, $Pb(OH)_2$, and PbF_2, were obtained. They not only repair the surface defects of $CsPbBr_3$ nanocrystals but also stabilize the phase structure of the inner $CsPbBr_3$ core by constructing a core–shell like structure. The photoluminescence thermal resistance experiments show that the treated sample could preserve 79% of its original emission intensity up to 373 K, far superior to that (17%) of pristine $CsPbBr_3$. Based on the thermally stable $CsPbBr_3$ nanocrystals, we achieved temperature-stable white LED devices with a stable electroluminescence spectrum, color gamut and color coordinates in thermal stress tests (up to 373 K).

Received 24th November 2021
Accepted 27th February 2022

DOI: 10.1039/d1sc06554h

rsc.li/chemical-science

Introduction

Lead halide perovskite nanocrystals (NCs) have emerged as outstanding emitters for light emitting diodes (LEDs) and backlight displays owing to their tunable narrow-band emission, high color purity, high defect tolerance, and superior photoluminescence quantum yields (PLQYs).[1–4] In the past few years, there have been breakthroughs in the performance of perovskite based LED devices, such as high efficiency, wide color gamut and cost competitiveness.[5–7] The rapid development of perovskite LEDs has led to achieving an external quantum efficiency (EQE) of 23.4% at green wavelengths with excellent operating stability (with an EQE of 45.5% based on a hemispherical lens).[8] Despite recent rapid progress, one critical bottleneck to the practical applications of perovskite LEDs is the instability of perovskite NCs, which derives from their intrinsically moisture/light/oxygen/heat sensitive ionic structures and low formation energy.[9,10] So far, many great efforts have been made to enhance the stability of perovskite NCs against moisture/light/oxygen, and substantial progress has been obtained, including compact barrier matrix encapsulation (SiO_2,[11] Al_2O_3,[12] TiO_2,[13] polymeric matrices,[14] *etc.*) and surface engineering strategies.[15,16] However, another often overlooked problem of perovskite NCs is the severe drop in luminescence intensity with increasing temperature (so-called fluorescence thermal quenching), leading to a very adverse impact on practical display application.[17–20] Actually, LED devices inevitably generate heat during operation, and their temperature can easily reach 373 K or even higher,[21] which causes the PL emission thermal quenching behaviors of perovskite NCs and leads to color deviation and brightness weakening of the display screen. Therefore, exploring efficient strategies for realizing high PL emission at elevated temperatures and suppressing the thermal quenching of perovskite NCs is very urgent for their practical applications in LEDs.

Generally, the thermal quenching of fluorescent materials is usually caused by their surface trap states or thermally activated carrier trapping and phonon-assisted non-radiative decay.[18,19,22] In the 1990s, Hines and Guyot-Sionnest proposed a passivation strategy to generate a stable layer with a wider band gap, so as to protect excitations from probing a defective surface.[23] Based on

[a]*School of Environmental Science and Engineering, Shanghai Jiao Tong University, Shanghai 200240, China. E-mail: liangli117@sjtu.edu.cn*

[b]*Department of Electronic Engineering, School of Electronics Information and Electrical Engineering, Shanghai Jiao Tong University, Shanghai 200240, China*

[c]*Shanghai Engineering Research Center of Solid Waste Treatment and Resource Recovery, Shanghai Jiao Tong University, Shanghai 200240, China*

† Electronic supplementary information (ESI) available: Experimental section, characterization details and additional figures and tables. See DOI: 10.1039/d1sc06554h

this concept, the thermal quenching problems of traditional CdSe quantum dots have been alleviated to a certain extent.[22,24] As for perovskite NCs, due to their low trapping activation energy, numerous defects will be inevitably generated with the increase in temperature, which results in a fast drop of PL emission. For example, all-inorganic $CsPbBr_3$ perovskite NCs heated to 373 K have been shown to suffer an over 80% fading of their room-temperature PL emission.[18,19,25] To this end, some breakthrough efforts have been proposed to suppress the serious PL emission thermal quenching of perovskite NCs.

Zou *et al.*[17] demonstrated an effective strategy through Mn^{2+} substitution to effectively increase the formation energy of $CsPbX_3$ (X = Cl, Br, I) NCs, achieving high thermotolerance and anti-thermal quenching of perovskite NCs. Recently, Liu *et al.*[18] proposed a fluoride ion post-synthesis treatment strategy that produces fluorine-rich surfaces with a wider bandgap than the inner $CsPbBr_3$ core, simultaneously greatly improving the trapping activation energy, achieving stable PLQY values of 90% up to 373 K and with no thermal quenching for successive thermal cycles. However, there are few reports on the in-depth mechanism of thermal quenching and corresponding universal strategies, which leads to the lack of regular and technical guidance for the universal suppression of thermal quenching. For classical colloidal perovskite NCs, in the heating process, colloidal perovskite NCs not only produced surface defects but also inevitably caused ion migration and agglomeration due to intrinsic structural instabilities, which makes it difficult to deeply explore the mechanism of thermal quenching and perform follow-up strategies to suppress thermal quenching. Excitingly, our previous work proposed a high-temperature solid-state method to realize the *in situ* encapsulation and ceramic-like stability of perovskite NCs.[26] In this all-solid-state synthesis, perovskite NCs were confined in the internal solid space of silica and isolated from each other, which prevented ion migration and induced particle fusion between NCs during the test with high thermal stress, and therefore, could be outstanding candidates to explore the mechanism of thermal quenching.

In this work, we have designed an anion passivation strategy based on new high temperature solid-state technology that can effectively passivate surface lead defects and suppress PL thermal quenching in $CsPbBr_3$ NCs. The introduced anions (such as SO_4^{2-}, OH^-, and F^- ions) can convert the surface lead of $CsPbBr_3$ NCs to wide-bandgap passivation layers with thermodynamical stability. The wide-bandgap passivation layers, such as $PbSO_4$, $Pb(OH)_2$, and PbF_2, not only repair the surface defects of $CsPbBr_3$ NCs, but also greatly improve the thermally activated trapping activation energy, and reduce the recombination probability of excitons and thermally activated defects, resulting in highly thermotolerant $CsPbBr_3$ NCs up to 373 K. Meanwhile, thanks to the complete encapsulation of dense SiO_2 during the high temperature solid-state reaction, the resulting $CsPbBr_3$ NCs exhibited extraordinary long-term stability in various environments (water, light, HCl solution, and NaOH solution) for up to 3600 hours without obvious PL emission decays. More surprisingly, the corresponding white LED backlight devices can still maintain the stability of the electroluminescence spectrum, color gamut, and color coordinates in thermal stress tests, providing a promising pathway to achieve brightness and color fidelity in real-world backlight displays.

Results and discussion

Thermal resistance performance

To suppress PL thermal quenching in $CsPbBr_3$ NCs, the wide-bandgap passivation layers must chemically and strongly bond to the perovskite surface. The chemically attached coating layers can passivate the surface defects by eliminating surface dangling bonds, and thus enhance the intrinsic luminescence and stability. More importantly, the wide-bandgap passivation layers with higher formation energy have mechanical rigidity, which can stabilize the phase structure of the inner $CsPbBr_3$ NCs and reduce high temperature induced defects. In the experiment, $CsPbBr_3$ NCs were synthesized by a template confined high temperature solid-state method as shown in Fig. S1.† First, mesoporous silica (MCM-41) was selected as the confined template, which can realize the confined growth of high quality $CsPbBr_3$ NCs. Next, perovskite precursors (CsBr and $PbBr_2$), and objective anion salts were first dissolved in water and mixed with mesoporous silica and then dried at 80 °C. The obtained solid powder was ground and calcined at 700 °C for 30 min in an argon atmosphere. Finally, the cooled samples were washed with ultrapure water and dried to obtain the anion-treated $CsPbBr_3$ NCs. In this case, the mole ratio of CsBr and $PbBr_2$ was always kept at 1 : 1. In order to form a stable passivation layer on the surface of $CsPbBr_3$ NCs, the introduced anions, such as SO_4^{2-}, OH^-, and F^- ions, can closely combine with surface lead (Pb^{2+}) to form an insulating layer, corresponding to $PbSO_4$, $Pb(OH)_2$, and PbF_2. The surface passivation layer formed strong chemical bonds with the $CsPbBr_3$ NCs and offered much better resistance to many harmful stimuli under continuous heating and high temperature. The compositions of the different samples were evaluated by energy-dispersive spectroscopy (EDS) and the content of perovskite nanocrystals encapsulated into SiO_2 was about 18 wt% (Tables S1–S4†). Next, we explored the effects of different anions on the optical properties of $CsPbBr_3$ NCs. In Fig. S2,† the optical absorption and PL spectra of pristine $CsPbBr_3$ and anion-treated $CsPbBr_3$ NCs showed they all almost have identical spectra including the spectral shape and positions. But, the addition of anions effectively enhanced the PLQY of $CsPbBr_3$ NCs. Upon increasing the anion : Pb ratio to 70%, the PLQYs of anion-treated $CsPbBr_3$ NCs all have been effectively improved. Further increasing the anion : Pb ratio to 100% or even higher will lead to a rapid decline in the PLQY, mainly due to the peeling off of the Pb^{2+} from $CsPbBr_3$ NCs by excessive anions, which means the reduction of the Pb^{2+} content in $CsPbBr_3$ NCs and results in the transformation of $CsPbBr_3$ into the Cs_4PbBr_6 phase (Fig. S3†). For this reason, in subsequent thermal resistance tests and structural studies, we focused on the comparison between pristine $CsPbBr_3$ NCs and anion-treated $CsPbBr_3$ NCs with anion : Pb ratio up to 70%.

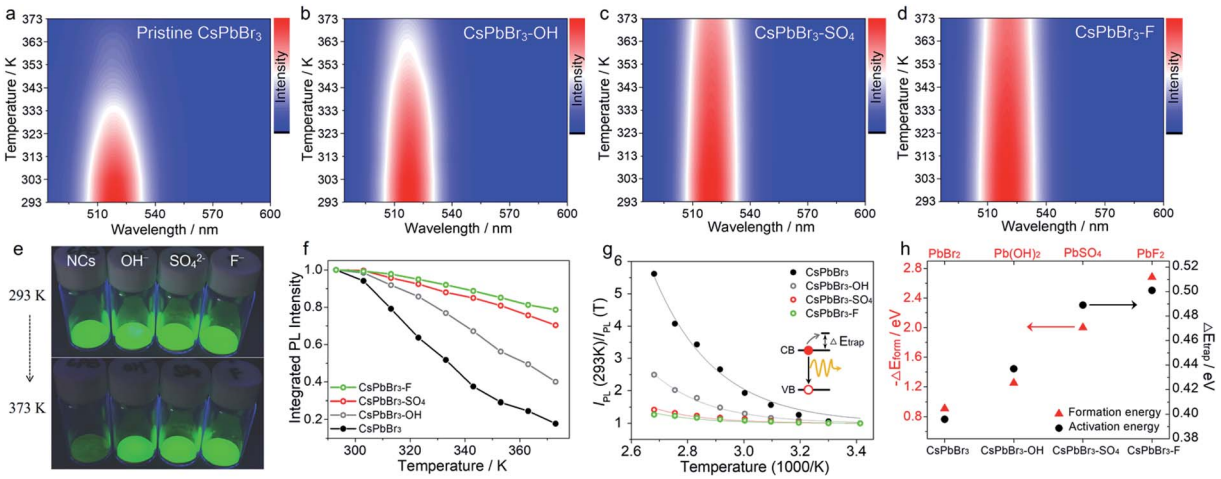

Fig. 1 Temperature-dependent PL spectra (excitation wavelength is 450 nm) of pristine $CsPbBr_3$ NCs (a), $CsPbBr_3$–OH NCs (b), $CsPbBr_3$–SO_4 NCs (c), and $CsPbBr_3$–F NCs (d) at increasing temperatures from 293 to 373 K. (e) Optical images of pristine and anion-treated $CsPbBr_3$ NCs heated on a hot plate at 293 and 373 K under UV excitation. (f) The integrated PL intensity of pristine and different anion treated $CsPbBr_3$ NCs. (g) Analysis of the PL intensity trend *versus* 1000/T fitted to a single-trap model. The solid lines are the fitting curves to eqn (1). (h) The trend for formation energy of different lead compounds and ΔE_{trap} values of different anion-treated $CsPbBr_3$ NCs.

Next, we evaluated the PL thermal quenching behavior of $CsPbBr_3$ NCs before and after anion (SO_4^{2-}, OH^-, and F^- ions) treatment. As shown in Fig. 1, pristine and anion-treated $CsPbBr_3$ NCs settled on the bottom of the glass bottle were placed on a hot plate at $T = 293$ K, respectively. When heated up to 373 K, the fluorescence of pristine $CsPbBr_3$ NCs decayed rapidly, but the anion-treated $CsPbBr_3$ NCs can still display bright green emission under UV light irradiation (Fig. 1e), indicating their excellent ability to suppress thermal quenching. To further quantitatively analyze the thermal quenching behavior, we monitored the *in situ* PL spectra of pristine and anion-treated $CsPbBr_3$ NCs during heating ramps from 293 to 373 K, as shown in Fig. 1a–d and S4.† The corresponding integrated PL intensities of the target samples (normalized to the respective value at 293 K) are shown in Fig. 1f. As for pristine $CsPbBr_3$ NCs, upon raising the temperature to 373 K, the PL intensity dropped sharply to ~17% of their original value at 293 K. Strikingly, the addition of anions (SO_4^{2-}, OH^-, and F^- ions) significantly strengthened the thermal resistance of $CsPbBr_3$ NCs, so that the PL intensities of $CsPbBr_3$–OH, $CsPbBr_3$–SO_4 and $CsPbBr_3$–F NCs could still be maintained above 40%, 70%, and 79% of their original PL intensities under thermal stress as high as 373 K, respectively (Fig. 1f). Therefore, the strategy for utilizing anions to build thermally stable passivation layers ($PbSO_4$, $Pb(OH)_2$, and PbF_2) can realize the remarkable PL thermal resistance of $CsPbBr_3$ NCs and maintain the emission efficiency under high-temperature working conditions. It should be noted that all the passivation reagents are potassium salts, leading to the introduction of K^+ ions that may play some roles in anti-thermal quenching. To clarify the influence of K^+ ions, KBr was selected to treat $CsPbBr_3$ NCs, and the thermal quenching of $CsPbBr_3$–KBr NCs is shown in Fig. S5.† Upon increasing the temperature to 373 K, the PL intensity of $CsPbBr_3$–KBr NCs dropped steeply to ~16% of their initial value at 293 K, which was similar to that of the original sample, basically ruling out the contributions of K^+ ions in the stabilization process. In this system, anions (SO_4^{2-}, OH^-, and F^- ions) played a more decisive role than cations (K^+), mainly due to the stable passivation layer derived from anions and surface lead.

Moreover, we found that there are some correlations between the type of anions and the suppression performance of thermal quenching in NCs. In general, the thermal quenching behavior of NCs or quantum dots is affected by their surface trap states or intrinsic trapping activation energy.[24,27] In this work, the suppression effects of the anions on thermal quenching follow a certain trend of $F^- > SO_4^{2-} > OH^- > Br^-$. From the viewpoint of chemistry, the four anions have different affinities to Pb^{2+} ($F^- > SO_4^{2-} > OH^- > Br^-$).[28,29] Therefore, we speculate that their ability to suppress thermal quenching is determined by the formation energy of the surface lead passivation layers. To further analyze the effect of the different anion treatments, the activation energy for carrier trapping (ΔE_{trap}) of target $CsPbBr_3$ NCs was estimated by fitting the temperature-dependent integrated PL intensity, through Arrhenius eqn (1):

$$I_{PL}(T) = \frac{I_{PL}^0}{1 + Ae^{-\Delta E_{trap}/k_B T}} \quad (1)$$

in which $I_{PL}(T)$ is the temperature-dependent integrated PL intensity, I_{PL}^0 is the initial PL intensity at 293 K, k_B is the Boltzmann constant, and A is a parameter related to the cross section of the trap state.[18,27] By fitting the high temperature induced PL loss of the target $CsPbBr_3$ NCs from 293 to 373 K (Fig. 1f), the corresponding fitting curves are shown in Fig. 1g, and the obtained ΔE_{trap} values for the $CsPbBr_3$ samples are listed in Fig. 1h and Table S5.† For pristine $CsPbBr_3$ NCs, the estimated ΔE_{trap} value was as low as 396 meV, which was caused by the inherent trap states of NCs. However, after anion treatment, the ΔE_{trap} values of $CsPbBr_3$ NCs have been greatly improved, reaching 437 meV, 489 meV, and 501 meV for

$CsPbBr_3$–OH, $CsPbBr_3$–SO_4, and $CsPbBr_3$–F, indicating that the NCs were effectively stabilized,[18] which was consistent with the above behavior of suppressing thermal quenching. Generally, the surface defects on the $CsPbBr_3$ NCs are mainly $PbBr_x$ or halide vacancies with dangling bonds. Consequently, treating the $CsPbBr_3$ NCs with anions can effectively passivate the halide vacancies or convert surface $PbBr_x$ into passivation layers with higher heat resistance. In this system, we summarized and compared the formation energies of different lead compound passivation layers, as shown in Fig. 1h and Table S6.†[28,29] As expected, the formation energy of $PbBr_2$ is the lowest, which makes $PbBr_2$ more prone to undergo chemical bond changes in a high temperature environment, such as lattice expansion or deformation and increased trap states, resulting in severe PL emission thermal quenching of NCs.

In contrast, the passivation layers with higher formation energy can effectively inhibit ion migration, keep the phase structure stable and reduce the defects of $CsPbBr_3$ NCs at high temperatures, thereby inhibiting non-radiative recombination and improving anti-thermal quenching. Therefore, the trends of ΔE_{trap} values and formation energy of surface lead layers correlate nearly perfectly with each other (Fig. 1h), further confirming the speculated mechanism of the anion treatment in the excellent thermal resistance of the $CsPbBr_3$ NCs.

Notably, to further demonstrate our concept, the target anion treatments were also applied to colloidal $CsPbBr_3$ NCs without careful optimization (Fig. 2 and S6†). In this case, initial colloidal $CsPbBr_3$ NCs were synthesized by the hot-injection method.[18] Then, a certain amount of the anion salt solution was added to the $CsPbBr_3$ toluene solution with stirring for 30 min at room temperature. Finally, the anion-treated colloidal $CsPbBr_3$ NCs solution was obtained *via* centrifugation. The post treatment resulted in a substantial enhancement of the thermal resistance, demonstrating the universality of the proposed strategy. It should be noted that, in the colloidal NC system, colloidal $CsPbBr_3$–OH NCs cannot be obtained, because the strong base will rapidly destroy the surface ligands of NCs and cause PL quenching. After treatment with SO_4^{2-} and F^- ions, the treated $CsPbBr_3$ NCs showed excellent thermal resistance, as shown in Fig. 2, following a similar trend ($F^- > SO_4^{2-} > Br^-$).

In-depth mechanism insights for suppressing thermal quenching

All the above results showed that the target anions can effectively improve the trapping activation energy and anti-thermal quenching of $CsPbBr_3$ NCs. To understand the mechanism, we took pristine $CsPbBr_3$ NCs and SO_4^{2-}-treated $CsPbBr_3$ NCs as examples, and performed a series of temperature-dependent *in situ* characterization studies to confirm the proposed mechanism of surface lead passivation and a wide-bandgap surface layer for suppressing thermal quenching.

In situ UV-vis absorption spectra were obtained to monitor photoinduced exciton evolutions of $CsPbBr_3$ NCs at different temperatures from 293 to 373 K (Fig. 3a and b). With the increase in temperature, the absorption band edges of both pristine and SO_4^{2-}-treated $CsPbBr_3$ NCs remained almost unchanged, but the intensity of their exciton absorption peaks had changed significantly. The stabilities of excitons are determined by external factors such as temperature and carrier concentration.[30,31] In this case, high temperature can lead to exciton decomposition and broadening of the exciton absorption peak, resulting in fluorescence decay or even quenching. By comparison, when the temperature increased to 373 K, the exciton absorption peak of the pristine $CsPbBr_3$ NCs became widened significantly, while the SO_4^{2-}-treated $CsPbBr_3$ NCs still

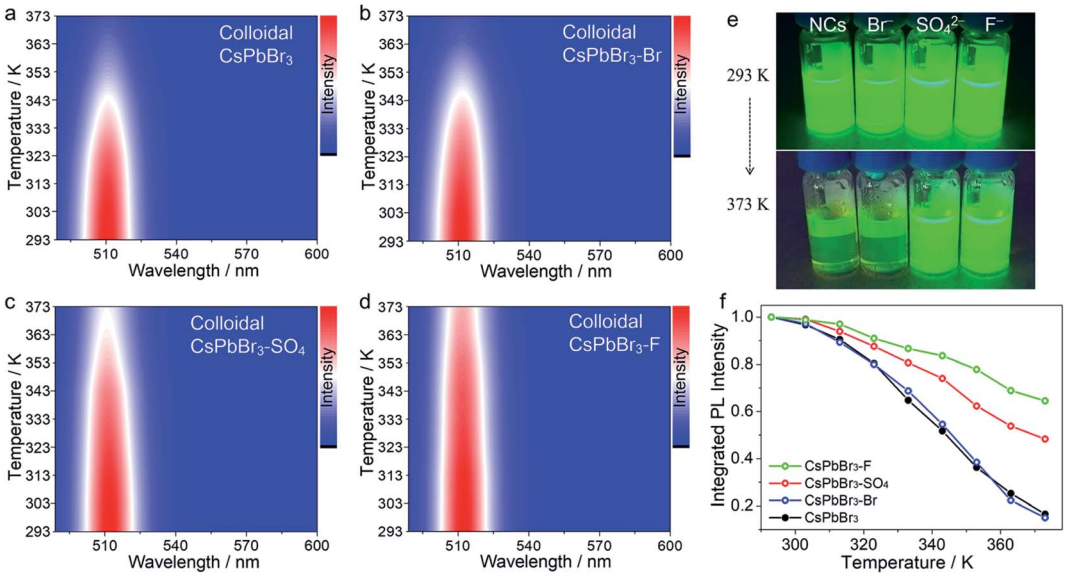

Fig. 2 Temperature-dependent PL spectra (excitation wavelength is 450 nm) of colloidal $CsPbBr_3$ NCs (a), colloidal $CsPbBr_3$–KBr NCs (b), colloidal $CsPbBr_3$–SO_4 NCs (c), and colloidal $CsPbBr_3$–F NCs (d) at increasing temperatures from 293 to 373 K. (e) Optical images of pristine and anion-treated colloidal $CsPbBr_3$ NCs upon heating on a hot plate at 293 and 373 K under UV excitation. (f) The integrated PL intensity of pristine and different anion treated colloidal $CsPbBr_3$ NCs.

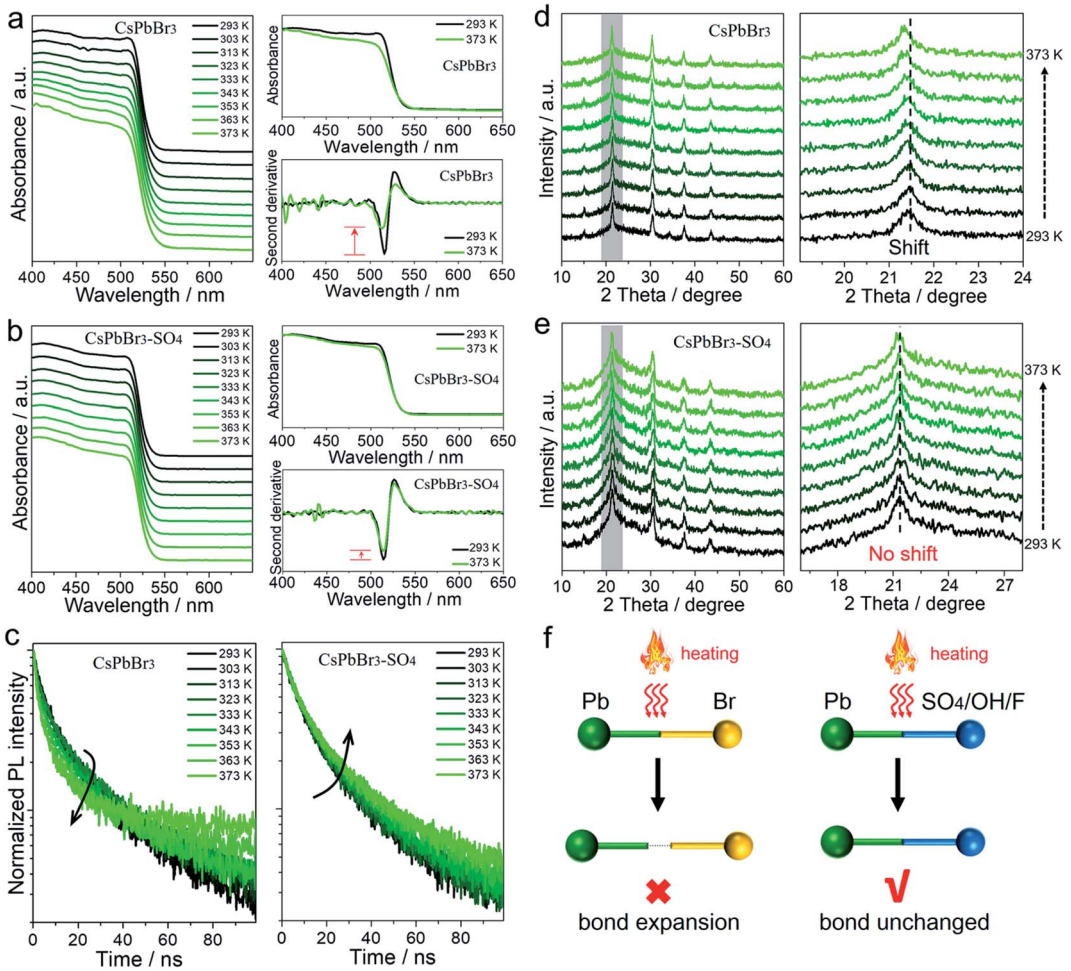

Fig. 3 Temperature-dependent *in situ* characterization studies for pristine and SO_4^{2-}-treated $CsPbBr_3$ NCs at increasing temperatures from 293 to 373 K. (a and b) *In situ* UV-vis absorption spectra and treatment of the absorption spectra with the second derivative, (c) *in situ* PL lifetime decay curves, and (d and e) *in situ* XRD patterns. (f) Schematic diagram of the suggested mechanism for thermal stability.

maintained the initial shape of the absorption peak (Fig. 3a and b). To visually observe the evolution of the exciton absorption peak, we treated the absorption spectra of NCs with the second derivative as shown in Fig. 3a and b. Obviously, the decay values of the exciton absorption peak for pristine $CsPbBr_3$ NCs were sharper than that of $CsPbBr_3$–SO_4 NCs. We reported the PL intensity of pristine and SO_4^{2-}-treated $CsPbBr_3$ NCs during five thermal cycles between $T = 293$ and 373 K, as shown in Fig. S7.† The results showed that the thermal quenching behavior was perfectly reversible, which eliminated the permanent or irreversible destruction of the perovskite structure under thermal stress. Therefore, the observed thermal quenching behavior was purely caused by the surface state of the single $CsPbBr_3$ NCs. Pristine $CsPbBr_3$ NCs have more surface defects, and high temperature will also induce extra defects, such as lattice expansion/distortion, surface ion migration, *etc.*, which will make excitons easier to capture by defects at high temperature, leading to severe PL decay at high temperature. As for the $CsPbBr_3$–SO_4 sample, on the one hand, SO_4^{2-} ion treatment can effectively passivate the surface defects, improve the trapping activation energy, stabilize the structure and inhibit the generation of defects at high temperature; on the other hand, the wide-bandgap $PbSO_4$ passivation layer on the surface of NCs can confine the excitons and remain stable at high temperature, leading to reduced quenching of PL emission.

In situ PL lifetime decay curves were obtained to evaluate the trap state evolutions during the rise in temperatures (Fig. 3c), and the exponential fitting results are listed in Tables S7–S8.† For pristine $CsPbBr_3$ NCs, with the rise in temperature, the average PL lifetime τ_{ave} dropped from 25.08 ns to 13.40 ns, implying that carrier trapping was strongly enhanced at elevated temperatures. The accelerated PL kinetics decay originated from the thermally activated escape of carriers to various defects at elevated temperatures, such as halogen vacancies and lead defects, according to previous reports.[18,19,24,27] Thanks to SO_4^{2-} ion treatment, the average PL lifetimes of $CsPbBr_3$–SO_4 NCs increased slightly from 24.50 ns to 29.66 ns due to thermally activated delayed fluorescence during the heating process.[19,27] Therefore, the SO_4^{2-} ion passivation strategy can effectively eliminate trap states and reduce the non-radiative recombination path by constructing a $PbSO_4$ passivation layer, which was consistent with the high remaining PL.

In situ XRD was carried out to monitor the crystal structure evolutions of $CsPbBr_3$ NCs before and after SO_4^{2-} passivation during temperature ramps from 293 to 373 K (Fig. 3d and e). Upon increasing the temperature to 373 K, both pristine and SO_4^{2-}-treated $CsPbBr_3$ NCs still present diffraction peaks corresponding to the cubic phase of the $CsPbBr_3$ crystal, showing that increasing the temperature up to 373 K will not promote the derivation of other phases from $CsPbBr_3$. After careful analysis, the XRD diffraction peaks of pristine $CsPbBr_3$ NCs shifted toward lower angles with the increase in temperature, meaning that the lattice spacing increased at high temperature, which derived from the bond lengthening and lattice expansion of the $CsPbBr_3$ crystal at high temperature. However, XRD diffraction peaks of $CsPbBr_3$–SO_4 NCs remained almost unchanged when the temperature increased from 293 to 373 K. *In situ* XRD of pure $PbSO_4$ samples during temperature ramps from 293 to 373 K (Fig. S8†) showed that the diffraction peaks of $PbSO_4$ remained almost unchanged when the temperature increased from 293 to 373 K, indicating that lattice expansion can be ignored at 373 K. Therefore, we suspect that the thermally stable $PbSO_4$ passivation layers with higher formation

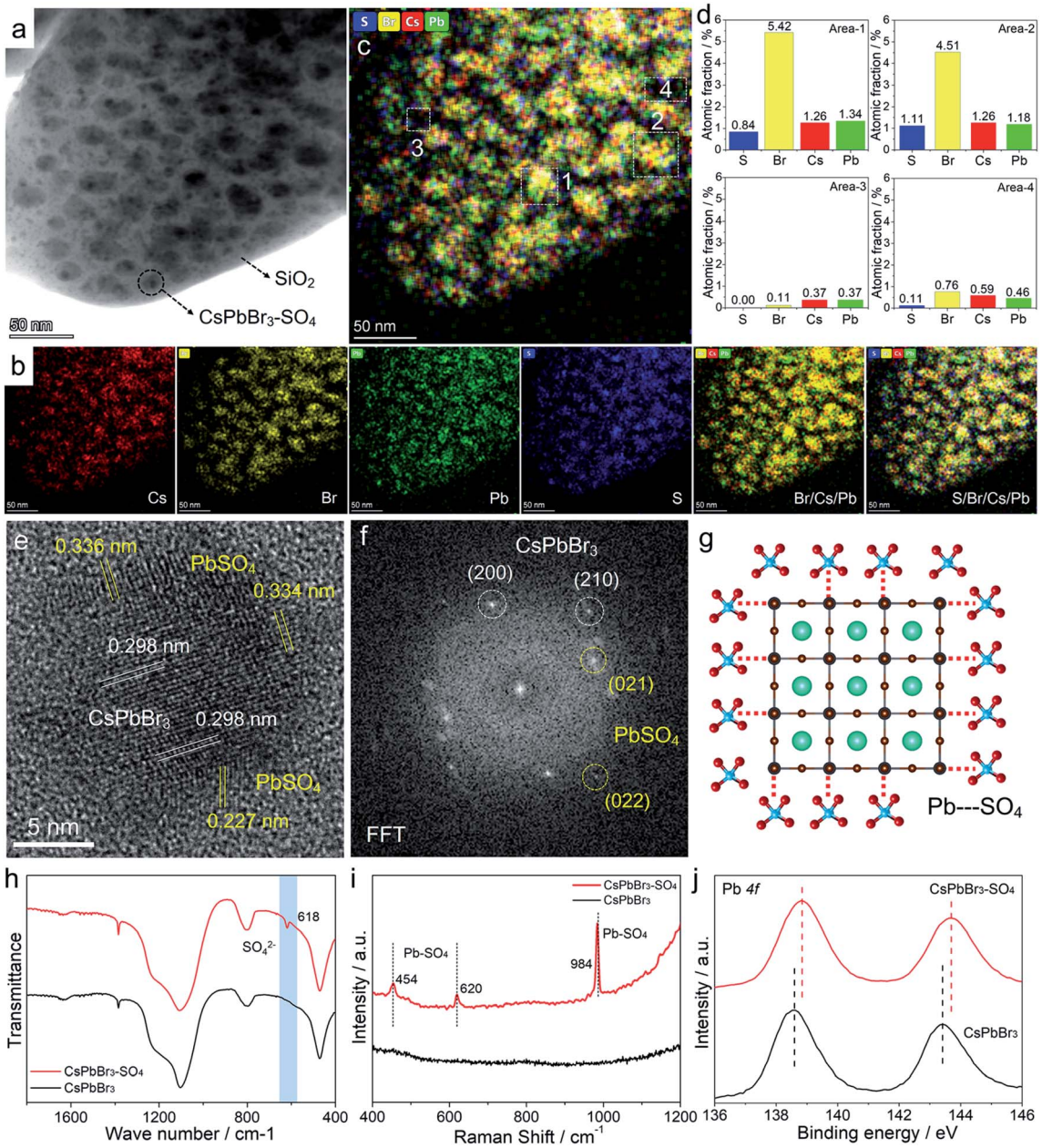

Fig. 4 (a and b) TEM image and the corresponding elemental mapping images of the $CsPbBr_3$–SO_4 sample. (c and d) Mixed elemental mapping image and the corresponding EDS results of different areas. (e and f) HR-TEM image and the corresponding FFT image of $CsPbBr_3$–SO_4 NCs. (g) Schematic diagram of the $CsPbBr_3$–$PbSO_4$ core–shell structure. (h) FT-IR spectra, (i) Raman spectra, and (j) XPS spectra of Pb 4f for pristine and SO_4^{2-}-treated $CsPbBr_3$ NCs.

energy can act as a rigid shell to stabilize and suppress the high-temperature induced lattice expansion of inner $CsPbBr_3$ NCs.

Transmission electron microscopy (TEM) images (Fig. 4a and S9–S11†) of pristine $CsPbBr_3$ NCs and $CsPbBr_3$–SO_4 NCs showed that $CsPbBr_3$ NCs were uniformly distributed in the collapsed SiO_2 system. The scanning electron microscopy (SEM) images of $CsPbBr_3$–SO_4 showed that the surfaces of the sample were smooth without impurities through the water washing step (Fig. S12†), which also indicated that the $CsPbBr_3$ NCs were indeed encapsulated inside the SiO_2 system. And the average sizes of pristine $CsPbBr_3$ NCs and $CsPbBr_3$–SO_4 NCs were 10.5 nm and 12.3 nm, respectively, and the increased size of $CsPbBr_3$–SO_4 NCs may be caused by the formation of the $PbSO_4$ layer. The high-angle annular dark-field scanning transmission electron microscopy (HAADF-STEM) image and its corresponding elemental mappings of $CsPbBr_3$–SO_4 (Fig. 4a, b and S10†) revealed that the Cs, Pb, Br, and S elements were distributed in $CsPbBr_3$ NCs. Furthermore, we carried out energy-dispersive spectroscopy (EDS) on the samples to accurately determine the location and content of the S element, as shown in Fig. 4c, d and S13–S14.† We selected four points in TEM for EDS analysis, and the results showed that the S element mainly existed on the $CsPbBr_3$ NCs, while there was almost no S element in the blank area (without $CsPbBr_3$ NCs) in the system (Fig. 4c and d), indicating that SO_4^{2-} ions were indeed adsorbed on $CsPbBr_3$ NCs and tended to combine with Pb^{2+} to form the $PbSO_4$ passivation layer. The high-resolution TEM (HR-TEM) image and the corresponding fast Fourier transform (FFT) pattern were used to further verify the core–shell like structure. As for pristine $CsPbBr_3$ NCs, the samples showed a regular perovskite lattice, which belonged to the cubic phase (Fig. S9†). Obviously, compared with pristine $CsPbBr_3$ NCs, there were more diffraction points in $CsPbBr_3$–SO_4, which belonged to $PbSO_4$ and $CsPbBr_3$ NCs (Fig. 4e, f and S15†). And the HR-TEM images revealed that $PbSO_4$ formed at the edge of the NCs had a periodic lattice, indicating that the $PbSO_4$ layer was tightly coated on the surface of $CsPbBr_3$ NCs to construct a typical core–shell like structure. Therefore, the role of the introduced SO_4^{2-} ions was to mainly combine with the surface lead of the $CsPbBr_3$ NCs to form a more stable $PbSO_4$ passivation layer,[32] as shown in Fig. 4g. After careful comparison, we found that the characteristic XRD peaks of $PbSO_4$ appeared in the system when the doping content of SO_4^{2-} ions was increased to 70% (Fig. S3†). The Fourier transform infrared (FT-IR) spectra (Fig. 4h and S16†) of the SO_4^{2-} treated sample showed a characteristic vibration peak at 618 cm^{-1} ascribed to the tetrahedral structure of SO_4^{2-} ions, indicating the formation of strong ionic bonds between Pb^{2+} and SO_4^{2-} ions;[32] and the Raman spectra[33] (Fig. 4i) further confirmed that the SO_4^{2-}-treated $CsPbBr_3$ NCs presented the characteristic peaks of $PbSO_4$ at around 454, 620, and 984 cm^{-1}, which appropriately correspond to the pure $PbSO_4$ standard sample (Fig. S17†). X-ray photoemission spectroscopy (XPS) measurements based on the washed samples further corroborated the perovskite surface composition after SO_4^{2-} treatment.[32] First, the S 2p spectra confirmed the presence of SO_4^{2-} ions in treated NCs (Fig. S18†), and the Pb 4f spectra revealed noticeable differences between pristine $CsPbBr_3$ NCs and SO_4^{2-}-treated $CsPbBr_3$ NCs (Fig. 4j). After SO_4^{2-} treatment, the Pb peaks of $CsPbBr_3$–SO_4 NCs shifted toward higher binding energies, indicating the formation of stronger ionic bonding between Pb^{2+} and SO_4^{2-} ions. Therefore, the above solid evidence, including HR-TEM, FT-IR, Raman, and XPS spectra, all confirmed that the surfaces of $CsPbBr_3$ NCs were converted to a wide-bandgap $PbSO_4$ passivation layer through the reaction with SO_4^{2-} ions. Similarly, the introduced F^- ions and OH^- ions can also form stable passivation layers on the surface of $CsPbBr_3$ NCs (Fig. S19–S20†).

Based on the above analysis, we have speculated the mechanism of the anion passivation strategy to suppress thermal quenching, as shown in Fig. 3f. In short, for untreated NCs, high temperature can induce or accelerate surface ion migrations, which produced more surface defects, thereby increasing non-radiative recombination paths and causing PL emission thermal quenching. After being treated by the target anions, the thermally stable passivation layers ($PbSO_4$, $Pb(OH)_2$, and PbF_2) can act as a rigid shell to stabilize and suppress the high-temperature induced ion migration of $CsPbBr_3$ NCs, meanwhile effectively repairing surface defects and improving the trapping activation energy, yielding reduced non-radiative recombination paths and suppressed PL emission thermal quenching.

Temperature-stable white light-emitting diodes

It is worth emphasizing that the above experiments and discussions have verified that the anion-treated $CsPbBr_3$ NCs presented excellent high-temperature resistance, which was very considerable for practical display application. For this purpose, we fabricated proof-of-concept white light-emitting diode (WLED) devices with SO_4^{2-}-treated $CsPbBr_3$ NCs as the active materials, and preliminarily explored their performance at different operating temperatures (Fig. 5 and S21†). The WLED devices were prepared by encapsulating green-emitting $CsPbBr_3$ NCs and commercial red-emitting KSF (K_2SiF_6:Mn^{4+}) phosphors onto the blue emitting GaN chip (wavelength: 450 nm). As for pristine $CsPbBr_3$ NCs (Fig. 5a and Table S9†), the corresponding WLED devices displayed white light emission at room temperature (293 K), and the CIE color coordinates were optimized at (0.3309, 0.3561). However, when the operating temperature gradually rose to 373 K, the CIE color coordinates shifted significantly from the initial (0.3309, 0.3561) to (0.3756, 0.2469), representing purplish pink luminescence, due to the thermal quenching of the green light components ($CsPbBr_3$ NCs) at high temperatures (Fig. 5b). The WLED devices based on $CsPbBr_3$–SO_4 NCs can still display quasi white light emission even at a high temperature of 373 K, corresponding to the color coordinates at (0.3676, 0.3130), as shown in Fig. 5c and Table S10.† And the WLED devices can maintain a stable electroluminescence spectrum in thermal stress tests (Fig. 5d). Furthermore, the color gamut of the WLED devices based on $CsPbBr_3$–SO_4 NCs had only a slight attenuation at 373 K, from 130.7% to 128.5% (Fig. S21†), meaning that the corresponding display screen can maintain uniform brightness and color fidelity in the working environment.

Meanwhile, aside from the excellent thermal stability, thanks to the complete encapsulation of dense SiO_2 during the

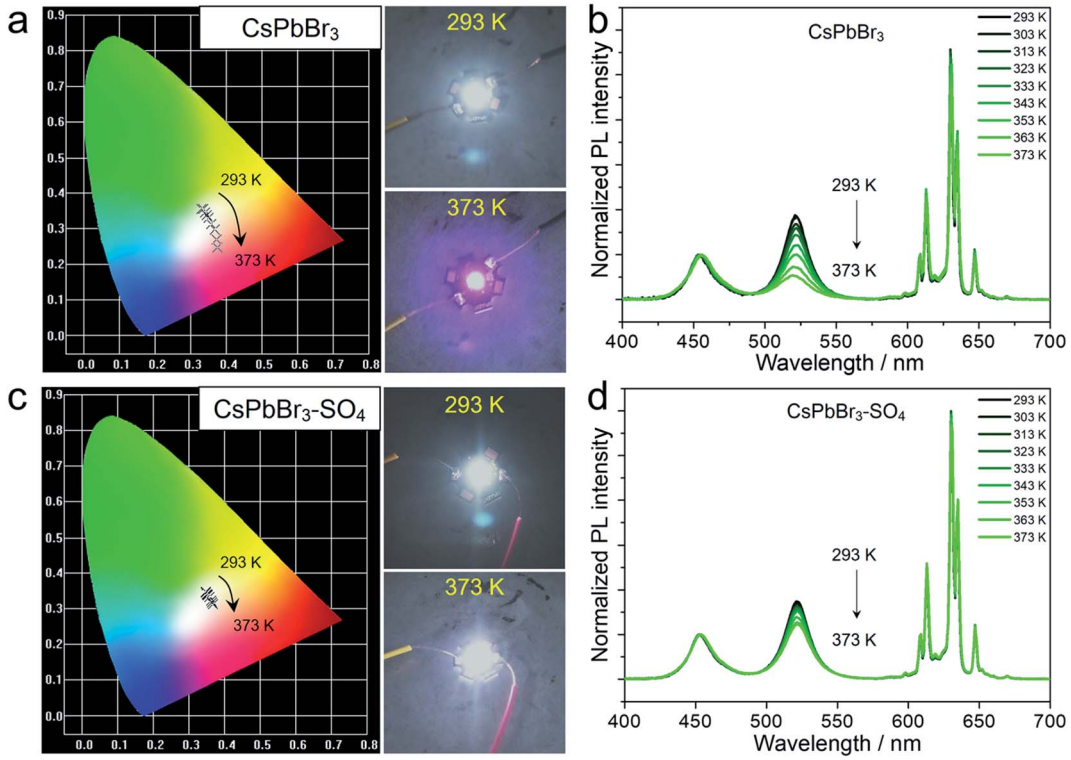

Fig. 5 (a and b) The WLED based on pristine $CsPbBr_3$ NCs. (a) The color coordinates of the WLED at increasing temperatures from 293 to 373 K, inset: photographs of the WLED operated at 293 K and 373 K. (b) The emission spectrum of the WLED at increasing temperatures from 293 to 373 K. (c and d) The WLED based on $CsPbBr_3$–SO_4 NCs. (c) The color coordinates of the WLED at increasing temperatures from 293 to 373 K, inset: photographs of the WLED operated at 293 K and 373 K. (d) The emission spectrum of the WLED at increasing temperatures from 293 to 373 K.

high-temperature solid-state reaction, the resulting sealed $CsPbBr_3$ NCs exhibited extraordinary long-term chemical and photo stabilities in various environments (water, light, HCl solution, and NaOH solution) for up to 3600 hours without obvious PL emission decays (Fig. S22–S24†).

Conclusions

In summary, we have demonstrated the anion passivation strategy that can convert the surface lead of $CsPbBr_3$ NCs to thermally stable passivation layers to suppress emission thermal quenching behavior and improve the thermal stability of the $CsPbBr_3$ structure. Temperature-dependent *in situ* characterization studies, including XRD, UV-vis absorption spectra, and PL lifetime, were performed to deeply evaluate the origin of thermal quenching and the mechanism of suppressing thermal quenching by the coating of wide-bandgap passivation layers. We finally confirmed that suppressing the thermal quenching is greatly related to the formation energy of surface lead passivation layers following the order of PbF_2 >$PbSO_4$ >$Pb(OH)_2$ > $PbBr_2$. By this anion assisted high-temperature solid-state synthesis, we simultaneously solved the universal chemical and photo stability problems of $CsPbBr_3$ NCs. On the one hand, the dense SiO_2 encapsulation successfully protects $CsPbBr_3$ NCs from some factors that can quench photoluminescence, such as moisture, oxygen, and ion migration. On the other hand, by using wide-bandgap passivation layers, the trapping activation energy of $CsPbBr_3$ NCs was significantly enhanced, which allows $CsPbBr_3$ NCs to achieve a thermally stable electroluminescence spectrum, color gamut, and color coordinates at high temperatures. Therefore, we believe that our research results have great guiding significance for the practical application of LED devices or backlight displays in the future.

Data availability

All characterization data are available in the ESI.† Raw data are available from the corresponding authors.

Author contributions

Q. Z. and L. L. proposed the original research idea. The manuscript was co-written by L. L. and Q. Z. The experiments, including nanocrystal synthesis, thermal quenching experiments, LED encapsulation and the stability test were performed by Q. Z., M. H., Q. W., W. Z., M. L., C. Z., X. L., and W. Z. Q. Z., L. K. and X. G performed the structural characterization. All the authors discussed the results, interpreted the findings, and reviewed the manuscript.

Conflicts of interest

There are no conflicts of interest to declare.

Acknowledgements

This work was supported by the National Key R&D Program (2018YFC1800600); the National Natural Science Foundation of China (NSFC 22175113, 42007125); the China Postdoctoral Science Foundation (2021M702115); the Guangdong Province's 2018-2019 Key R&D Program (2019B010924001); Shanghai Jiao Tong University Scientific and Technological Innovation Funds.

References

1 T. Chiba, Y. Hayashi, H. Ebe, K. Hoshi, J. Sato, S. Sato, Y.-J. Pu, S. Ohisa and J. Kido, *Nat. Photonics*, 2018, **12**, 681–687.
2 H. Tsai, S. Shrestha, R. A. Vilá, W. Huang, C. Liu, C.-H. Hou, H.-H. Huang, X. Wen, M. Li and G. Wiederrecht, *Nat. Photonics*, 2021, 1–7.
3 C. Zhang, Q. Wan, B. Wang, W. Zheng, M. Liu, Q. Zhang, L. Kong and L. Li, *J. Phys. Chem. C*, 2019, **123**, 26161–26169.
4 C. Zhang, S. Wang, X. Li, M. Yuan, L. Turyanska and X. Yang, *Adv. Funct. Mater.*, 2020, **30**, 1910582.
5 S. Pimputkar, J. S. Speck, S. P. DenBaars and S. Nakamura, *Nat. Photonics*, 2009, **3**, 180–182.
6 M. V. Kovalenko, L. Protesescu and M. I. Bodnarchuk, *Science*, 2017, **358**, 745–750.
7 Q. Zhang, X. Sun, W. Zheng, Q. Wan, M. Liu, X. Liao, T. Hagio, R. Ichino, L. Kong and H. Wang, *Chem. Mater.*, 2021, **33**, 3575–3584.
8 Y.-H. Kim, S. Kim, A. Kakekhani, J. Park, J. Park, Y.-H. Lee, H. Xu, S. Nagane, R. B. Wexler and D.-H. Kim, *Nat. Photonics*, 2021, **15**, 148–155.
9 Y. Wei, Z. Cheng and J. Lin, *Chem. Soc. Rev.*, 2019, **48**, 310–350.
10 Q. Zhang, W. Zheng, Q. Wan, M. Liu, X. Feng, L. Kong and L. Li, *Adv. Opt. Mater.*, 2021, **9**, 2002130.
11 S. Huang, Z. Li, L. Kong, N. Zhu, A. Shan and L. Li, *J. Am. Chem. Soc.*, 2016, **138**, 5749–5752.
12 Z. Li, L. Kong, S. Huang and L. Li, *Angew. Chem.*, 2017, **129**, 8246–8250.
13 Z. J. Li, E. Hofman, J. Li, A. H. Davis, C. H. Tung, L. Z. Wu and W. Zheng, *Adv. Funct. Mater.*, 2018, **28**, 1704288.
14 Z. Wang, R. Fu, F. Li, H. Xie, P. He, Q. Sha, Z. Tang, N. Wang and H. Zhong, *Adv. Funct. Mater.*, 2021, **31**, 2010009.
15 G. H. Ahmed, J. Yin, O. M. Bakr and O. F. Mohammed, *ACS Energy Lett.*, 2021, **6**, 1340–1357.
16 K. Hills-Kimball, H. Yang, T. Cai, J. Wang and O. Chen, *Adv. Sci.*, 2021, 2100214.
17 S. Zou, Y. Liu, J. Li, C. Liu, R. Feng, F. Jiang, Y. Li, J. Song, H. Zeng and M. Hong, *J. Am. Chem. Soc.*, 2017, **139**, 11443–11450.
18 M. Liu, Q. Wan, H. Wang, F. Carulli, X. Sun, W. Zheng, L. Kong, Q. Zhang, C. Zhang and Q. Zhang, *Nat. Photonics*, 2021, **15**, 379–385.
19 Q. Zhang, Z. Li, M. Liu, L. Kong, W. Zheng, B. Wang and L. Li, *J. Phys. Chem. Lett.*, 2020, **11**, 993–999.
20 C. Bi, S. Wang, Q. Li, S. V. Kershaw, J. Tian and A. L. Rogach, *J. Phys. Chem. Lett.*, 2019, **10**, 943–952.
21 V. Bachmann, C. Ronda and A. Meijerink, *Chem. Mater.*, 2009, **21**, 2077–2084.
22 X. Yuan, J. Zheng, R. Zeng, P. Jing, W. Ji, J. Zhao, W. Yang and H. Li, *Nanoscale*, 2014, **6**, 300–307.
23 M. A. Hines and P. Guyot-Sionnest, *J. Phys. Chem.*, 1996, **100**, 468–471.
24 Y. Zhao, C. Riemersma, F. Pietra, R. Koole, C. de Mello Donegá and A. Meijerink, *ACS Nano*, 2012, **6**, 9058–9067.
25 X. Li, Y. Wu, S. Zhang, B. Cai, Y. Gu, J. Song and H. Zeng, *Adv. Funct. Mater.*, 2016, **26**, 2435–2445.
26 Q. Zhang, B. Wang, W. Zheng, L. Kong, Q. Wan, C. Zhang, Z. Li, X. Cao, M. Liu and L. Li, *Nat. Commun.*, 2020, **11**, 31.
27 B. T. Diroll, G. Nedelcu, M. V. Kovalenko and R. D. Schaller, *Adv. Funct. Mater.*, 2017, **27**, 1606750.
28 A. Jain, S. P. Ong, G. Hautier, W. Chen, W. D. Richards, S. Dacek, S. Cholia, D. Gunter, D. Skinner and G. Ceder, *APL Mater.*, 2013, **1**, 011002.
29 S. P. Ong, W. D. Richards, A. Jain, G. Hautier, M. Kocher, S. Cholia, D. Gunter, V. L. Chevrier, K. A. Persson and G. Ceder, *Comput. Mater. Sci.*, 2013, **68**, 314–319.
30 D. Lubyshev, P. González-Borrero, E. Marega Jr, E. Petitprez, N. La Scala Jr and P. Basmaji, *Appl. Phys. Lett.*, 1996, **68**, 205–207.
31 G. Han, B. Chen, L. Zuo, K. Xue, P. Chen, Y. Duan and Y. Zhao, *Org. Electron.*, 2016, **37**, 207–212.
32 S. Yang, S. Chen, E. Mosconi, Y. Fang, X. Xiao, C. Wang, Y. Zhou, Z. Yu, J. Zhao and Y. Gao, *Science*, 2019, **365**, 473–478.
33 B. Han, A. Xie, Q. Yu, F. Huang, Y. Shen and L. Zhu, *Appl. Surf. Sci.*, 2012, **261**, 623–627.